# Metal−Support Interaction and Redox Behavior of Pt(1 wt %)/Ce$_{0.6}$Zr$_{0.4}$O$_2$

**Giulio Deganello, Francesco Giannici, Antonino Martorana,\* Giuseppe Pantaleo, and Antonio Prestianni**

*Dipartimento di Chimica Inorganica e Analitica "Stanislao Cannizzaro", Università di Palermo, viale delle Scienze, I-90128 Palermo, Italy*

**Antonella Balerna**

*Istituto Nazionale di Fisica Nucleare, Laboratori Nazionali di Frascati, via Enrico Fermi 44, I-00044 Frascati, Italy*

**Leonarda F. Liotta and Alessandro Longo**

*Consiglio Nazionale delle Ricerche, Istituto per lo Studio dei Materiali Nanostrutturati, Sezione di Palermo, via Ugo La Malfa, 153, I-90146 Palermo, Italy*

The catalyst Pt(1 wt %)/Ce$_{0.6}$Zr$_{0.4}$O$_2$ is studied by CO-temperature programmed reduction (CO-TPR), isothermal oxygen storage complete capacity (OSCC), X-ray absorption spectroscopy (XAS) at the Pt L$_{III}$ edge, and in situ X-ray diffraction (in situ XRD), with the aim of elucidating the role of supported metal in CO oxidation by ceria-based three-way catalysts (TWC). The redox behavior of Pt(1 wt %)/Ce$_{0.6}$Zr$_{0.4}$O$_2$ is compared to that of bare ceria-zirconia. OSCC of redox-aged Pt/ceria-zirconia is twice that of bare ceria-zirconia, and the maximum of CO consumption occurs at a temperature about 300 K lower than redox-aged ceria-zirconia. XAS analysis allows one to evidence the formation of a platinum−cerium alloy in redox-aged samples and the stability of the metal particles toward oxidation and sintering during high-temperature treatments. Under CO flux at 773 K, bare ceria-zirconia shows a continuous drift of diffraction peaks toward smaller Bragg angles, due to a progressive increase of Ce(III) content. Under the same treatment, the structural rearrangement of Pt-supported ceria-zirconia starts after an induction time and takes place with an abrupt change of the lattice constant. The experimental evidence points to the role of supported Pt in modifying the redox properties of ceria-zirconia with respect to the bare support. It is proposed that the much faster bulk reduction observed by in situ XRD for redox-aged Pt/ceria-zirconia can be attributed to an easier release of reacted CO$_2$, producing a more effective turnover of reactants at the catalyst surface.

## Introduction

State-of-the-art three-way catalysts (TWC) for automotive exhaust abatement are constituted by noble metals (NM) supported on ceria-zirconia mixed oxides. In these systems, Ce(IV) can be easily reduced to Ce(III) with consequent release of oxygen in the reaction environment, a property usually referred to as oxygen storage capacity (OSC). A crucial point for the improvement of TWC performance is the effective oxidation of CO and unburned or partially burned hydrocarbons at low working temperature and in reducing environment.[1] In these conditions, typically met at the engine start-up, the metal−support interaction plays a fundamental role in improving the CO oxidation.

In this paper, in situ structural techniques, X-ray absorption spectroscopy (XAS) and X-ray diffraction (XRD), are used to investigate the interaction of Pt nanoparticles with a Ce$_{0.6}$Zr$_{0.4}$O$_2$ mixed oxide. The structural data are integrated by temperature programmed reduction with CO (CO-TPR) and oxygen storage complete capacity (OSCC) measurements, to ascertain correlations with catalytic performances.

Several authors studied by different techniques the mechanism of oxygen delivery by ceria-based oxides.[2−5] In some instances, the attention was focused on the peculiar behavior of NM-supported ceria and ceria-zirconia and in particular on the investigation of metal−support interaction.[2,3,6,7] Concerning this issue, it is generally understood that reacting species are preferentially absorbed onto NM crystallites and that the catalytic sites for oxidation are located at the metal−oxide boundary:[8] according to this interpretation, a back-spillover of oxygen from the support to the NM particle can be involved in CO oxidation.[9] On the other hand, Hardacre and collaborators found that a Pt/ceria model catalyst, where the metal particles were totally embedded in the oxide matrix, showed very good performance in CO oxidation and therefore proposed that the oxide itself is modified by the interaction with the metal, becoming the effective catalyst for oxidation reactions; this conclusion was corroborated by the LEED observation of a Pt$_5$-Ce alloy.[6] The formation of the Pt$_5$Ce alloy was also detected by Bernal et al. for Pt/CeO$_2$ samples reduced at 1173 K.[7] The hypothesis that the real catalytic site results from the interaction of platinum with the support surface found experimental evidence in the work of Fu et al., who observed that Pt supported on ceria continued to be active for the water gas-shift reaction

\* Corresponding author. Phone: 0039 091 489841. Fax: 0039 091 427584. E-mail: cric2@unipa.it.

also after leaching the metal phase by $CN^-$ and concluded that the catalytic sites are constituted by $Pt^{2+}$ and $Pt^{4+}$ species atomically dispersed in the oxide matrix.[10]

The possibility that some kind of strong metal−support interaction (SMSI) is operative in TWCs and affects the catalytic properties was put forth by different authors,[2,3,11−13] although there is not a general agreement about the beneficial or detrimental effect of such an interaction. Aiming at a structural characterization of the metal−support interface, we carried out in situ XAS experiments on the Pt $L_{III}$ edge of a Pt/ceria-zirconia catalyst. There are a few XAS studies on ceria-based three-way catalysts: some were focused on the local environment of Ce and Zr in ceria-zirconia TWCs,[14,15] while other authors investigated the supported precious metal. Bera et al. demonstrated by EXAFS (extended X-ray absorption fine structure) analysis an interaction $Pt^{2+}−O−Ce^{4+}$ in a $Pt/CeO_2$ sample prepared by combustion synthesis.[16] Bitter et al. performed in situ XANES (X-ray absorption near edge structures) measurements on a 7 wt % $Pt/CeO_2$ catalyst treated at different temperatures and demonstrated that the metal−support interaction determines a change of the Pt electronic structure when reduction treatment at 773 K is performed, while at higher temperatures decoration by $CeO_2$ of Pt particles takes place.[17] Finally, Longo et al. described the design of a new cell for in situ XAS measurements in transmission and fluorescence geometry and reported, as a case study, preliminary results about the Pt−support interaction in the catalytic system Pt(1 wt %)/$Ce_{0.6}Zr_{0.4}O_2$.[18]

The effect of lattice oxygen delivery to the reaction environment is actually the reduction of the ceria-zirconia mixed oxide. The influence of the metal−support interaction on the reduction of ceria-zirconia is investigated in this paper by in situ XRD experiments carried out during the anaerobic oxidation of CO by the Pt(1 wt %)/$Ce_{0.6}Zr_{0.4}O_2$ catalyst and by bare $Ce_{0.6}Zr_{0.4}O_2$ at 773 K. At this temperature, on the basis of the diffusion coefficients of oxygen in ceria-zirconia, the CO conversion is not limited by oxygen diffusion,[19] and therefore the influence of supported Pt on reactivity can be discriminated. Time-resolved XRD studies were performed by Ozawa and Loong on various TWC systems,[20] by Rodriguez et al. on ceria and ceria-zirconia,[21] and by Martorana et al. on Pt/ceria-zirconia.[22] The possibility to monitor the process of ceria-zirconia reduction by in situ XRD relies on the larger ionic radius of Ce(III) with respect to that of Ce(IV). Assuming that a linear relation exists between the cationic radii and the cell size,[23] it is possible to determine the Ce(IV)/Ce(III) relative amount and therefore to calculate the amount of bulk oxygen delivered by ceria-zirconia for the oxidation of CO. Comparison between the different redox behavior of Pt-supported and metal-free ceria-zirconia allows one to obtain evidence about the role of Pt in modifying the properties of the oxide.

### Experimental Section

**Synthesis Route.** $Ce_{0.6}Zr_{0.4}O_2$ support was prepared by the sol−gel method from $Zr(OCH_2CH_2CH_3)_4$ (70 wt % solution in *n*-propanol) and $Ce(NO_3)_3 \cdot 6H_2O$ (99.999%), dissolved in absolute ethanol, as precursors.[24] The hydrolysis of the zirconium propoxide was accomplished by the structural water present in the cerium salt at 333 K. Gelation occurred in about 12 h, and then the gel was evaporated to dryness under vacuum, heated in an oven at 423 K for 12 h, and calcined in air at 873 K for 4 h. The so prepared ceria-zirconia oxide shows a surface area of 56 $m^2/g$; in this paper, it is referred to as c-CZ. The Pt (1 wt %) was added by impregnation of the support with the calculated

amount of Pt(acetylacetonate)$_2$ solution in toluene at 343 K. After vacuum pumping, the solid was calcined at 673 K for 4 h to remove residual organic ligands; the so-obtained sample is labeled as c-Pt1CZ. A portion of c-Pt1CZ was subjected to two successive reduction/oxidation cycles (up to 1273 K with 5% $H_2$/Ar and up to 773 K with 5% $O_2$/He, respectively), to stabilize the ceria-zirconia phase in a homogeneous fluorite-type solid solution with composition $Ce_{0.6}Zr_{0.4}O_2$.[13] The resulting material is called r-Pt1CZ. The same treatment on c-CZ produced also a homogeneous fluoritic structure, labeled as r-CZ. The redox-cycled samples have a surface area (by BET) of about 15 $m^2/g$.

**CO-TPR and OSCC Experiments.** Temperature-programmed reduction (TPR) with CO was carried out with a Micromeritics Autochem 2910 apparatus connected to a mass quadrupole (Thermostar, Balzers) and an IR analyzer (ABB Uras 14) for monitoring the CO conversion and $CO_2$ formation. The reagent gas mixture consisting of 3300 ppm CO in He was led over 50 mg of catalyst at a flow rate of 50 mL min$^{-1}$, equivalent to a WHSV (weight hourly space velocity) of 60 000 mL h$^{-1}$ g$^{-1}$. CO-TPR tests were made by heating from room temperature to 1323 K. Before the tests, the samples were pretreated "in situ" under flowing 5% $O_2$/He at 773 K for 30 min, to eliminate any impurity on the surface and to ensure the full oxidation of the catalyst; He was then flowed at 773 K for 10 min to clean the reaction environment. Aiming at determining the maximum reducibility of the samples at selected temperatures,[25] OSCC measurements were performed isothermally at 473, 593, 773, and 973 K, in the same experimental conditions as CO-TPR tests. The OSCC was quantified in $\mu$mol of CO/(g catalyst) and calculated from the area enclosed between the background level and the CO consumption trace as a function of time during isothermal CO treatments. The sequence was repeated two times to investigate aging effects. After each OSCC measurement, the sample was oxidized at 773 K for 30 min and then He was flowed at 773 K for 10 min.

**In Situ X-ray Absorption.** The cell for in situ X-ray absorption experiments was described in a recent paper.[18] It allows one to make treatments on the investigated sample in the temperature range from 150 to 773 K and to put the sample in a suitable gas environment. Leaving the sample in the cell, it is possible to carry out X-ray absorption experiments in transmission or in fluorescence geometry. The data can be collected at low temperature, to reduce the dynamical contribution of the Debye−Waller factor, or at nonambient temperature to investigate the behavior of the sample in specific environments. It is also possible to scan the absorption edge in quick-XANES mode, to monitor sample changes in real time.

The sample r-Pt1CZ was mixed with boron nitride and pressed to form a pellet. The X-ray absorption experiments were carried out at the Pt $L_3$ edge (11 565 eV) in fluorescence geometry. The fresh catalyst was measured at liquid nitrogen temperature and also subjected to a reductive treatment in situ in CO/He at 773 K. The maximum duration of the treatment was 45 min, the time necessary for a noticeable decrease in $CO_2$ production.[18] The XAS experiments on the reduced samples were performed at 150 K after 15 and 45 min of treatment. After the 15′ treatment, a reoxidation was performed and the sample was measured at 150 K. Each reduction or oxidation treatment was followed by 10′ He flux cleaning.

Data extraction and EXAFS analysis were carried out by the GNXAS package.[26,27] This procedure allows one to analyze raw X-ray absorption spectra without the need for any pretreatment of the data such as EXAFS extraction and Fourier filtering. The

approach is based on a fitting procedure that optimizes the agreement between a model absorption signal $\alpha_{mod}(E)$ and the experimental one $\alpha_{exp}(E)$. The nonlinear multiparametric fit is performed by using the CERN library subroutine MINUIT, which allows one to carry out a detailed error analysis on the fitting parameters to achieve a good estimate of the confidence interval on the final results.[28] The model absorption is a function of the photon energy and is given by:

$$\alpha_{mod} = J\sigma_0(E)[1 + S_0^2\chi_{mod}(E - E_0) + \alpha_{background}(E) + \alpha_{excitation}(E)] \quad (1)$$

The EXAFS model $\chi_{mod}(E - E_0)$ is calculated according to the multiple scattering approximation (MS).[26] In the GNXAS analysis, the local atomic arrangement around the absorbing atom is decomposed into model atomic configurations $\gamma^{(2)}... \gamma^{(n)}$ containing 2, ..., n atoms, respectively. For each configuration, the atomic phase shifts are calculated using the most opportune exchange and correlation potentials in the muffin-tin approximation. The use of complex Hedin−Lundqvist potentials permits a correct inclusion of the effects due to inelastic losses. The contributions to the EXAFS signal are expressed in terms of irreducible n-body "$\gamma^{(n)}$" contributions, which are calculated considering the effects of all of the possible single and multiple scattering (MS) paths between the n-atoms. The theoretical EXAFS signal $\chi(k)$, where $k = [(2m_e/\bar{h}^2)\cdot(E - E_0)]^{1/2}$ is the modulus of the photoelectron wave vector, is given by the sum of the $\gamma^{(n)}$. The suitability of the model can be evaluated also by comparison of the Fourier transform of the experimental EXAFS signal, calculated in the whole measured k-interval, and of the sum of the model $\gamma^{(n)}$ functions. The parameter $S_0^2$ is a constant reduction factor for EXAFS intensity and accounts for an effective many-body correction to the one-electron cross section. $\sigma_0(E)$ is an arctangent steplike function accounting for the atomic cross section of the absorption of the atom of interest. The edge jump J accounts for the actual surface density of the photoabsorber atoms and is optimized by MINUIT. The background term $\alpha_{background}(E)$ is a smooth polynomial spline function accounting for the pre-edge and the post-edge contribution of all absorption channels. The knots position is defined in the analysis, while MINUIT optimizes the spline coefficients. The last term $\alpha_{excitation}(E)$ can take into account the possible multielectron excitation in the absorber atom adding one or more edges to the above-reported equation. The edge energy $E_0$ is refined in a range of $\pm 5$ eV around the maximum derivative of the absorption coefficient versus energy data.

**In Situ X-ray Diffraction.** The experimental setup for time-resolved XRD experiments at the GILDA beamline of ESRF was previously described.[29] In synthesis, an imaging-plate (IP) detector (Fuji, 200 × 400 mm$^2$) translates horizontally behind a vertical slit, so that a fresh IP surface is continuously exposed to the diffracted X-rays during sample treatments. The sample was loaded in a 1 mm diameter quartz capillary, fitted by an aluminum frame in a goniometer head. The capillary was open at both sides, allowing the reaction gases to flow through. To avoid gas flow blocking, the coarser powder fraction, with particles of diameters ranging from 80 to 120 $\mu$m, was obtained by meshing. A gas flux heater (Hot-air Blower, Cyberstar, Grenoble, France) with remote temperature control allows tuning of the sample temperature. An $\alpha$-alumina diffraction standard (NIST Standard Reference Material 676) was mixed with the sample to monitor (by thermal expansion of $\alpha$-alumina) the effective temperature in the capillary during high-temperature treatments and to determine with great accuracy the sample-
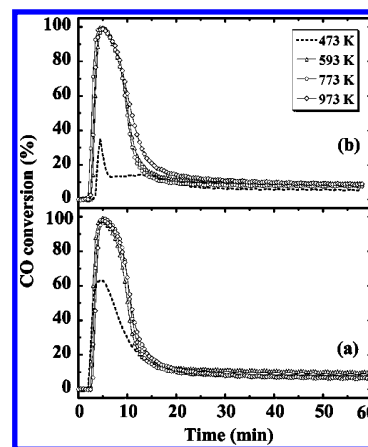


**Figure 1.** OSCC of c-Pt1CZ determined at the increasing temperatures indicated in the legend. (a) First cycle of treatments; (b) second cycle. At $t = 0$ s, the CO/He mixture is switched on, but the sample is bypassed to measure the instrumental baseline. At $t = 2$ min, the reagent is flowed on the sample and CO conversion starts with a few seconds delay.

to-detector distance. The XRD experiments were performed at fixed wavelength ($\lambda = 0.73286$ Å), with a beam size of 0.5 × 0.5 mm$^2$. The structural analyses were carried out by Rietveld refinement using the GSAS package.[30]

The in situ treatments are carried out isothermally at 773 K on r-CZ and on r-Pt1CZ sample. The samples are initially fluxed with a 10 vol % O$_2$/He mixture (20 mL/min) to ensure complete oxidation. Next, He is fluxed for 30′ to clean the reaction environment. During the last 10′ in He, the X-ray beam shutter is opened; thereafter, the reductive mixture CO 0.1%/He is fluxed at 20 mL/min while the XRD measurement is carried out. After the first reduction treatment, O$_2$ 10%/He is fluxed in the capillary. Once the reoxidation is done, the reduction−oxidation treatment is iterated at least one more time. Each change from reductive to oxidizing mixture (or vice versa) is preceded by a 5′ treatment in He flux.

## Results

**TPR-OSCC.** In agreement with previous BET, XRD, and XAS results, redox cycles produce in fresh ceria-zirconia oxide a decrease of specific surface and bring about a homogeneous bulk composition.[13,24,31] A similar behavior is observed also for Pt-supported ceria-zirconia. In Figure 1, isothermal CO conversion versus time is shown for c-Pt1CZ. The reduction mixture CO/He is sent on the fresh sample (Figure 1a) at increasing temperatures; after each reductive treatment, the sample is reoxidized according to the procedure described in the Experimental Section. The cycle of treatments from 473 to 973 K is then iterated, and the respective CO conversions are reported in Figure 1b. From comparison of the two cycles, it results that the fresh sample presents a larger CO conversion at 473 K, due to reaction of CO with Pt−O and Ce−O surface oxygens. This contribution depends on the larger surface area and Pt dispersion of the fresh sample and drastically decreases after the first thermal treatment. The CO conversions at temperatures higher than 473 K are similar, independently of the cycle. The same treatments to measure OSCC are carried out also on r-Pt1CZ. The corresponding data of CO conversion are reported in Figure 2; a larger operating window is evident at moderate and high temperatures (593−973 K), both in the first (Figure 2a) and in the second cycle (Figure 2b), with respect to the calcined sample.

CO-TPR traces are drawn in Figure 3. Figure 3a reports the CO-TPR profile of r-CZ. This material shows a single, slightly
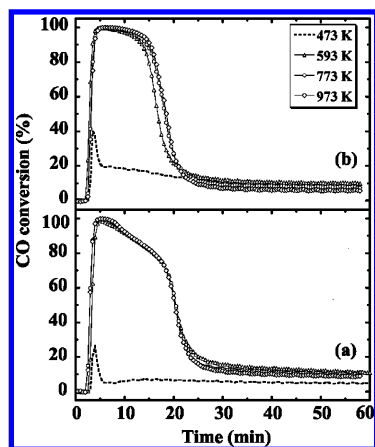
**Figure 2.** OSCC of redox-aged samples determined at the increasing temperatures indicated in the legend. (a) First cycle of treatments on r-Pt1CZ; (b) second cycle on r-Pt1CZ. After measurement of the baseline, the CO/He mixture is flowed on the sample at $t = 2$ min.
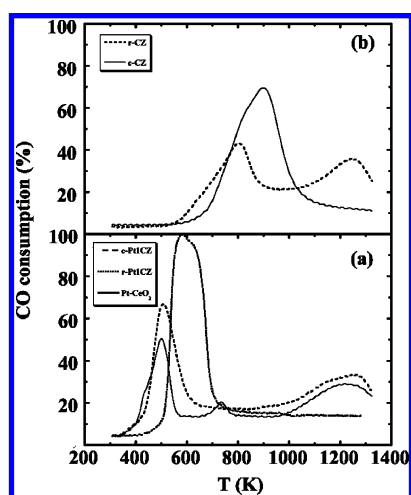


**Figure 3.** CO consumption curves versus temperature. (a) Pt-supported samples; (b) metal-free ceria-zirconia.

asymmetric, reduction peak centered at about 900 K. This evidence is in agreement with previous observations, indicating that TPR profiles of single-phase ceria-zirconia oxides generally display a single reduction peak.[32] The corresponding Pt-supported sample (Figure 3b) presents also a single peak, shifted 300 K toward lower temperatures.[13] The TPR trace of c-CZ (Figure 3a) is similar to that of pure ceria, indicating a possible segregation of ceria.[33] The c-CZ reduction peak centered at about 800 K shifts at about 500 K by Pt deposition (Figure 3b), while the reduction peak above 1000 K is not modified by supported Pt. Again, this behavior is similar to that of Pt−CeO$_2$ (Figure 3b), corroborating the hypothesis of ceria segregation in non redox-aged CZ.

**XAFS.** The interaction between platinum and ceria-zirconia is investigated by X-ray absorption spectroscopy. The r-Pt1CZ sample is analyzed as-prepared, after 15 min of reduction treatment in CO, after a reoxidation treatment on the 15′ reduced sample, and, finally, by a reduction lasting 45 min. As monitored by mass spectrometry, in correspondence to the 45′ treatment the CO$_2$ yield decreases to a background value, likely corresponding to the consumption of the available bulk oxygen. Table 1 accounts for the EXAFS analysis in the above-reported conditions. The fitting to the extracted EXAFS signals and the corresponding FT obtained by GNXAS are drawn in Figures 4 and 5, respectively. As reported in Table 1, in the as-prepared and reoxidized samples a Pt−O interaction is necessary for

**TABLE 1: EXAFS Analysis Relative to the r-Pt1CZ Sample Subjected to the Indicated Treatments**[a]

|  | as-prepared | 15 min | reoxidized | 45 min |
|---|---|---|---|---|
| | | Metallic Phase | | |
| $N_1$ | $7.5 \pm 0.5$ | $8.4 \pm 0.3$ | $7.2 \pm 0.3$ | $8.5 \pm 0.3$ |
| $R_1$ | $2.74 \pm 0.02$ | $2.75 \pm 0.02$ | $2.74 \pm 0.03$ | $2.75 \pm 0.03$ |
| $\sigma_1^2$ (Å$^2$) | $4.9 \pm 0.5$ | $4.9 \pm 0.5$ | $4.9 \pm 0.5$ | $4.9 \pm 0.5$ |
| $N_2$ | $4.2 \pm 0.7$ | $4.8 \pm 0.7$ | $4.2 \pm 0.5$ | $4.6 \pm 0.5$ |
| $R_2$ (Å) | $3.89 \pm 0.04$ | $3.89 \pm 0.04$ | $3.89 \pm 0.04$ | $3.89 \pm 0.04$ |
| $\sigma_2^2$ (Å$^2$) | $7.1 \pm 0.6$ | $7.1 \pm 0.5$ | $7.2 \pm 0.5$ | $6.5 \pm 0.5$ |
| $\theta_{120}$ | $120 \pm 4$ | $120 \pm 2$ | $120.0 \pm 3$ | $120.0 \pm 3$ |
| $\theta_{120}^2$ | $2.0 \pm 0.5$ | $2.2 \pm 0.5$ | $1.7 \pm 0.6$ | $1.8 \pm 0.6$ |
| | | Pt$_5$Ce Phase | | |
| $N_1$ | $1.6 \pm 0.7$ | $1.8 \pm 0.6$ | $1.4 \pm 0.5$ | $1.6 \pm 0.4$ |
| $R_1$ (Å) | $3.05 \pm 0.05$ | $3.03 \pm 0.04$ | $3.03 \pm 0.02$ | $3.04 \pm 0.03$ |
| $\sigma_1^2$ (Å$^2$) | $4.0 \pm 0.5$ | $3.8 \pm 0.06$ | $3.5 \pm 0.2$ | $3.5 \pm 0.4$ |
| | | Oxide Phase | | |
| $N_1$ | $1.0 \pm 0.4$ | | $2.0 \pm 0.7$ | |
| $R_1$ (Å) | $1.93 \pm 0.02$ | | $1.94 \pm 0.04$ | |
| $\sigma_1^2$ (Å$^2$) | $1.2 \pm 0.7$ | | $1.9 \pm 0.5$ | |

[a] The $\sigma^2$ Debye−Waller factors are given in $10^{-3}$ Å$^2$ units. $\theta_{120}$ and $\theta_{180}$ are the refined angles between the three body paths accounting for the third and fourth metallic phase coordination shell; $\sigma_{120}$ and $\sigma_{180}$ are the respective angle variances.
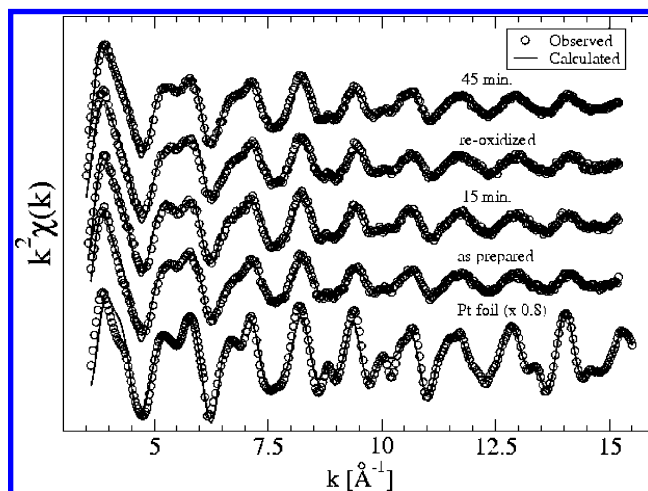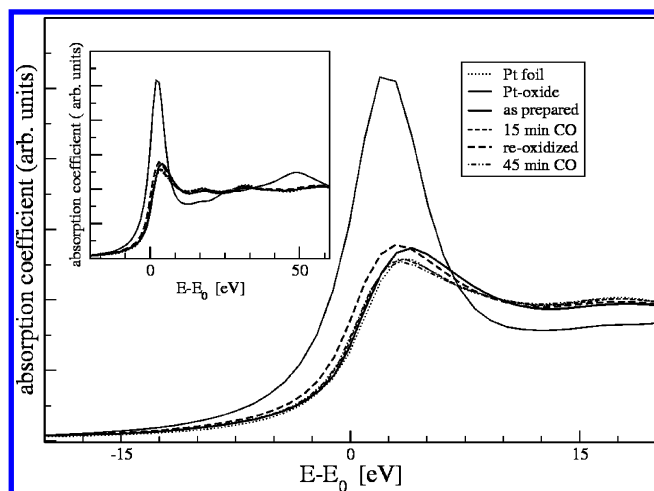


**Figure 4.** Extracted EXAFS signals (○) and calculated spectra (−) fitted to the data.
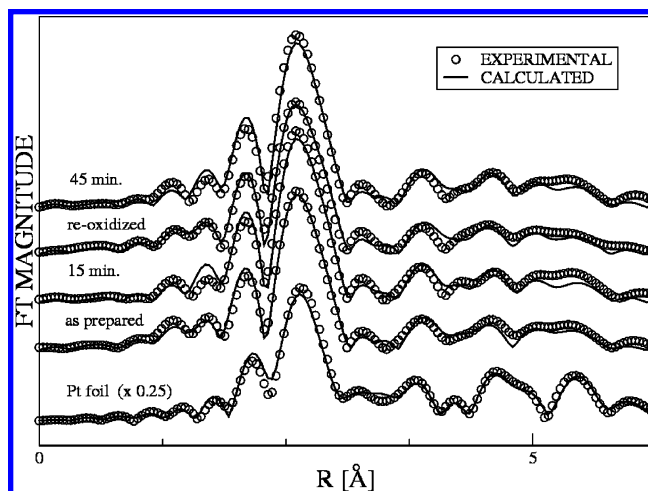


**Figure 5.** Fourier transform magnitude of the data (○) and of the calculated spectra (−) reported in Figure 4.

achieving a good fitting of the experimental signal. The XANES spectra are shown in Figure 6. The data are reported as a function of $E - E_0$, where $E_0$ is the threshold energy obtained

**Figure 6.** Pt L$_3$ edges of the r-Pt1CZ sample in correspondence to the indicated treatments. The inset shows the XANES up to 50 eV after edge.
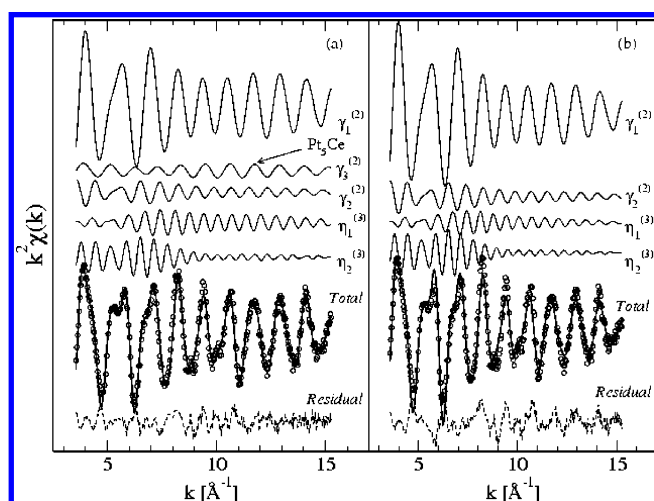


**Figure 7.** Component signals and overall fitting to the r-Pt1CZ EXAFS data. Two-body components are indicated by $\gamma_i^{(2)}$ and three-body components by $\eta_i^{(3)}$. (a) Allowing for a Pt−Ce contribution; (b) without Pt−Ce. The residual in panel b clearly shows that a well-defined frequency is missing.

as the maximum of the first derivative of the absorption data. The data are normalized for the atomic background and pre-edge-subtracted. By comparison, it is evident that the as-prepared and the reoxidized samples show a slight, but clearly visible, shift toward the $E_0$ of the PtO$_2$ reference sample. In Table 1, all of the samples, no matter the oxidation state, show evidence of a phase characterized by a direct Pt−Ce interaction. The components and the overall calculated and observed EXAFS patterns are shown in Figure 7a for the 45′ reduced sample. Figure 7b shows that a direct Pt−Ce interaction is essential to achieve a good fitting to the experimental EXAFS signal. Actually, the need of a signal with a well-defined frequency can be appreciated from the residual drawn in Figure 7b and is confirmed by the comparison between the Fourier transforms of the calculated and experimental EXAFS spectra, with and without the Pt−Ce interaction, respectively drawn in Figure 8a and b.

**In Situ XRD.** Figures 9 and 10 display the redox behavior of r-CZ and r-Pt1CZ, respectively, according to in situ X-ray diffraction. It can be seen that during reduction the diffraction peaks of r-CZ (Figure 9, in particular, shows the 220 peak of r-CZ and, as a reference, an α-alumina peak) drift toward smaller angles, due to a rise of lattice constant clearly associated
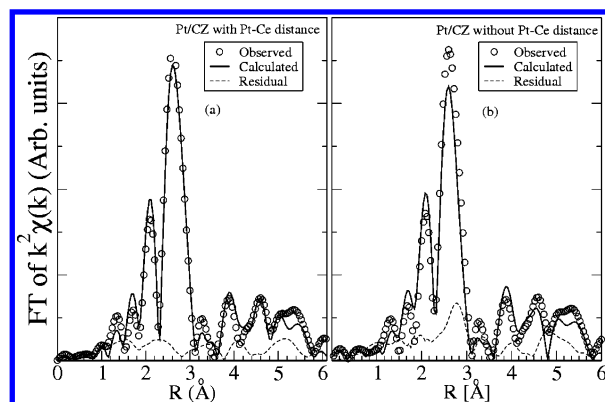


**Figure 8.** Fourier transform magnitude of the experimental and calculated EXAFS signals shown in Figure 7. (a) With the Pt−Ce distance; (b) without. Also, in the FTs the need of an additional frequency component in correspondence to the Pt first coordination shell is evident.
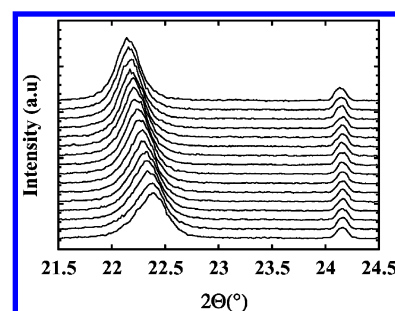


**Figure 9.** In situ XRD patterns of r-CZ. The patterns are recorded at 773 K in 20 mL/min CO 0.1%/He flow. The 220 ceria-zirconia peak is monitored at time frames of 4′. As a reference, one of the diffraction peaks of α-Al$_2$O$_3$ is also included. It is evident that α-alumina does not change, while the ceria-zirconia 220 peak progressively shifts to lower angles.
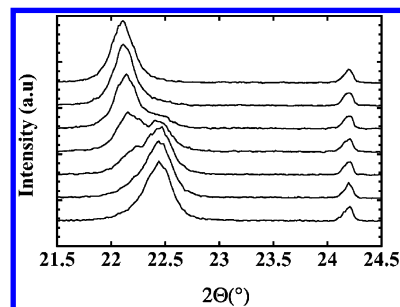


**Figure 10.** In situ XRD patterns of r-Pt1CZ. The patterns are recorded at 773 K in 20 mL/min CO 0.1%/He flow. The 220 ceria-zirconia peak is monitored at time frames of 60″. As a reference, one of the diffraction peaks of α-Al$_2$O$_3$ is also included. It is evident that α-alumina does not change, while ceria-zirconia suddenly changes from the oxidized to the reduced phase. During the transition, the simultaneous presence of both phases is clearly detectable.

with an increase of Ce(III) content.[20−22] The process begins at CO/He switching on and lasts for the whole duration of the in situ XRD experiment (about 1 h). The behavior of r-Pt1CZ is completely different (Figure 10). The change of lattice constant is accomplished in a few minutes; during the transition two CZ phases, one reduced and one still oxidized, are clearly detectable.

In Figure 11, the variation of the cubic lattice constant $a$ (actually, only the cationic sublattice is cubic, so that the ceria-zirconia lattice is also referred to as "pseudocubic")[33] of r-CZ (Figure 11a) and of the fwhm (full width at half maximum) of the 220 peak (Figure 11b) versus time during reduction−oxidation−reduction treatments at 773 K is shown. The values
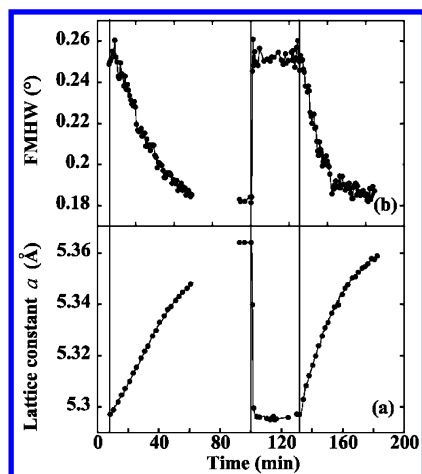
**Figure 11.** (a) Lattice constant *a* as a function of in situ treatment; (b) 220 peak fwhm of r-CZ. The changes of gases fed to the sample are indicated by vertical lines at 10′ (switching on of CO/He), 100′ (change to $O_2$/He), and 130′ (second reductive treatment). Each change of gas mixture is preceded by a 5′ treatment in He, to clean the reaction environment. The variation, both of lattice constant and fwhm, is progressive during reduction. During oxidation, these parameters vary very rapidly, and two phases, one still reduced and one oxidized, can be detected. The corresponding values of lattice constant and fwhm are weighted averages of these two phases.

of *a* are corrected for thermal expansion, so that the reported variations in the whole time interval are only due to the presence of reduced Ce(III) ions in the lattice. In the 0−60′ time interval, the reduction treatment is monitored by in situ XRD; during the subsequent 40 min, the reductive treatment keeps on while the XRD recording is interrupted. A 30 min oxidation is then accomplished. The recovery of the initial value of *a* during the oxidation process is very rapid, although this velocity is not directly comparable to that of the reduction process, as the composition of the $O_2$/He mixture is different. The subsequent reduction seems to be more straightforward with respect to the previous one, as can be seen by inspection of Figure 11a. A remarkable feature of the r-CZ time-resolved XRD patterns is that the fwhm during oxidation is definitely larger than the corresponding parameter during reduction and that this behavior is reversible and therefore not associated with sintering originated by thermal treatment.

The redox behavior of r-Pt1CZ is shown in Figure 12. Outside phase transition single values of lattice constant *a* (Figure 12a) and of fwhm (Figure 12b) are drawn; during redox transitions, as the Rietveld refinement requires two phases (Figure 10), the phase fraction-weighted averages of *a* and of fwhm are reported. An induction time (evidenced in Figure 12 by the vertical lines indicating the change to reductive gas mixtures) in the rise of lattice constant is systematically detected, although its length is different in the two reduction treatments. A sharp peak in fwhm is evident during the structural transitions of r-Pt1CZ.

## Discussion

The discussion of the experimental results is carried out separately for ceria-zirconia, calcined Pt/ceria-zirconia, and redox-aged Pt/ceria-zirconia. The section concerning r-Pt1CZ is also devoted to comparison with the other materials and general comments.

**Ceria-Zirconia.** Redox aging eliminates ceria segregation in CZ; this effect, already described in the literature, is demonstrated by XRD[22] and EXAFS[31] and confirmed by CO-TPR.[34] In fact, the TPR trace relative to r-CZ (Figure 3b) is character-
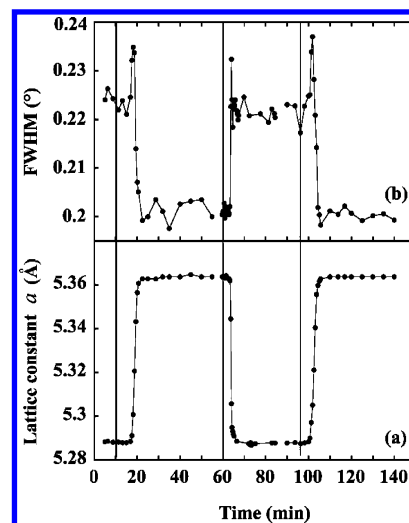


**Figure 12.** (a) Lattice constant *a* as a function of in situ treatment; (b) 220 peak fwhm of r-Pt1CZ. The changes of treatment gases are indicated by vertical lines at 10′ (switching on of CO/He), 60′ (change to $O_2$/He), and 90′ (second reductive treatment). Each change of gas mixture is preceded by a 5′ treatment in He, to clean the reaction environment. The variation of both lattice constant and fwhm is very quick. Outside the transition regions, the powder patterns are fitted with a single phase. During the transitions from the oxidized to the reduced phase and vice versa, two phases, one oxidized and one reduced, are necessary to perform the Rietveld refinement; the corresponding values of lattice constant and fwhm are weighted averages of these two phases.

ized by a single peak, while c-CZ (Figure 3b) behaves like pure ceria. In the latter material, the surface reduction starts at lower temperature, while bulk reduction takes place above 1000 K; on the contrary, in the redox-aged sample, surface and bulk reduction seem to approximately match. In situ XRD experiments provide evidence of bulk reduction in r-CZ (Figure 11a). The reduction process produces a progressive shift of the diffraction peaks (Figure 10), originated by the increasing amount of Ce(III) in the structure. At any intermediate state, the material is characterized by a unique cubic cell. The peak widths depend on the reduction state and are reversibly larger in the oxidized state and narrower in the reduced one (Figure 11b); therefore, sintering is not involved in the phenomenon and fwhm variation is likely dependent on strain release. This interpretation is in agreement with theoretical speculations, suggesting that the presence of the small zirconium atoms, which in the oxidized material produce strain in the structure and broadening of the diffraction peaks, is counterbalanced in the reduced state by the large Ce(III) ions.[34]

The reduction process of r-CZ is clearly originated at the surface, where the oxidation of CO involves the creation of surface oxygen vacancies and the reduction of Ce(IV) ions to Ce(III). To involve bulk processes, vacancies must diffuse into the bulk and, conversely, oxygen should emerge to the surface. The details of this mechanism have been a matter of speculation by Daturi and co-workers, who proposed that $F^+$ and F defects (anionic vacancies trapping, respectively, one and two electrons) are created at the surface by CO oxidation and that subsurface Ce(IV) is reduced by diffusion of these charged defects.[5] Although the duration of the XRD measurement did not allow one to monitor the whole reduction process, the lattice constant *a* of r-CZ in Figure 11a is likely approaching an asymptotic value of ∼5.36 Å. This value corresponds to a composition Ce-(IV)$_{0.3}$Ce(III)$_{0.3}$Zr$_{0.4}$O$_{1.85}$[22] and therefore to the reduction of about 50% of the available Ce(IV) ions; this Ce(III) amount is in good

agreement with the total OSC determined by thermogravimetry[35] and magnetic balance.[5]

As a final remark, careful comparison between the first and the second reduction cycle (Figure 11) shows that the latter is faster. This evidence could support the neutron diffraction analysis that oxygen ions in ceria-zirconia can be partly localized in octahedral sites and that the recovery of tetrahedral coordination after reoxidation could be hindered by the small size of zirconium ions.[4]

**Calcined Pt(1%)Ceria-Zirconia.** By inspection of Figure 3, the addition of Pt shifts the c-CZ low-temperature CO-TPR peak of about 300 K toward lower temperatures, while the high-temperature peak, associated with segregated ceria reduction, remains substantially unchanged. Therefore, supported Pt increases the reducibility of the surface; however, it is not effective in improving bulk reduction, if a uniform distribution of zirconium in the cerium oxide lattice is lacking. From analysis of the OSCC data relative to c-Pt1CZ (Figure 1), it is evident that the OSCC of the fresh sample at 473 K (Figure 1a) is higher than the OSCC relative to the second cycle (Figure 1b) at the same temperature. At this low reduction temperature, the OSCC is reasonably due to the reaction of CO with Pt−O and Ce−O available surface oxygens. The amount of oxygen released to the reaction environment is therefore dependent on platinum oxide dispersion and on ceria specific surface. The iterated reduction−oxidation cycles at increasing temperatures produce a collapse of the structure, with consequent decrease of surface area. This is likely the reason the OSCC relative to the second reduction run at 473 K (Figure 1b) is smaller. The similarity between the CO-TPR traces of c-Pt1CZ and of Pt(1 wt %)/ CeO$_2$ (Figure 3) is in agreement with this analysis, as c-Pt1CZ contains segregated ceria.[24] The EXAFS experiment carried out in situ on fresh c-Pt1CZ and reported in a previous paper shows that the EXAFS signal of the fresh sample can be interpreted on the basis of a Pt−O interaction proper of a disordered PtO$_2$ phase;[18] in the reduced sample, a Pt$^0$−Pt$^0$ distance is also necessary to fit the data. After reduction with CO at 773 K, the reoxidation treatment restores the disordered oxide environment of Pt. Therefore, it seems sound to conclude that the Pt phase in c-Pt1CZ is highly dispersed and in weak interaction with the support.

**Redox-Aged Pt(1%)Ceria-Zirconia.** Like c-Pt1CZ, the CO-TPR peak of r-Pt1CZ is shifted about 300 K with respect to the redox-aged support (Figure 3). In both r-CZ and r-Pt1CZ, the bulk reduction peak typical of ceria, c-CZ, and c-Pt1CZ drifts at lower temperatures and turns out to be almost merged with the surface reduction signal. According to the isothermal CO consumption traces (Figure 2), it is evident that r-Pt1CZ has a much wider operative window for CO oxidation with respect to c-Pt1CZ (Figure 1) and that the corresponding OSCC value is definitely larger. The smaller surface area of the redox-aged sample (15 m$^2$/g, by BET, as compared to 56 m$^2$/g of the calcined sample) is not detrimental for oxygen release, confirming that bulk oxygen is clearly involved in this process.

X-ray absorption experiments were carried out to obtain a structural characterization of the metal particles and to investigate the metal−support interaction in r-Pt1CZ. The dispersed, loosely bound Pt phase of c-Pt1CZ becomes, after redox aging, a well-grown and stable metal phase (Table 1). The metal crystallites could not be detected by X-ray diffraction, despite long exposures to the synchrotron radiation beam, due to very small particle size and lack of contrast with the support. It is likely that these features constitute a drawback also for transmission electron microscopy (TEM) analysis, although 3

nm Pt particles on CeO$_2$ were actually detected by TEM.[7] An estimate of the mean particle size based on the number of first neighbors as determined by EXAFS [36] gave an average size of about 1.5−1.8 nm, corresponding to about eight first neighbors (Table 1). It is worth noticing that this evaluation is in quite good agreement with small-angle X-ray scattering results.[13] Although other techniques are properly suited when possible, it should be remarked that EXAFS can yield reliable estimates in the range of very small particle size (<2 nm) and that in this range it ensures full sampling over the whole particle size distribution. A Pt particle size less than 2 nm is rather small and should give rise to easy oxidation at 773 K.[37] Actually, the only effect produced by oxidation treatments and detected by XAS is a minor Pt−O interaction, reversible under reduction environment, at a quite short distance (1.93 Å, Table 1). An even shorter distance (<1.9 Å) has been attributed, by DFT calculations, to a Pt−O interaction involving oxygen adsorbates on Pt clusters of a few atoms,[38] while experimental and theoretical results report a 1.93 Å Pt−O distance for oxygen adsorbed on a Pt(110) (1 × 2) surface.[39] The XANES spectra shown in Figure 6 confirm the presence of a Pt−O interaction that is absent in the reduced samples. Unlike c-Pt1CZ, the Pt$^0$−Pt$^0$ coordination shells (Table 1) of r-Pt1CZ remain substantially unaffected by redox treatments, demonstrating the high stability of the supported Pt particles under widely different environments. The absence of Pt particles sintering was already observed by other groups[25,40] and can constitute a hint that a stable metal−support interface is grown in r-Pt1CZ. The most striking evidence of this interaction is provided by the need of a Pt−Ce component necessary for a thoroughly satisfactory fitting of the EXAFS signal. The observed Pt−Ce distance (∼3.04 Å, Table 1) is definitely shorter than the 3.28 Å observed by Bera et al. and corresponding to a Pt−O−Ce interaction.[16] The $\gamma_2^{(2)}$ component drawn in Figure 7a is calculated using the Pt$_5$Ce phase described in the literature, and the optimized Pt−Ce distance is, within the error reported in Table 1, in fairly good agreement with the literature Pt−Ce first neighbors distance.[41] The possibility that Zr enters in the composition of the metal−support interface cannot be excluded; however, the EXAFS data do not allow one to obtain clear evidence concerning this issue. Taking into account that the bulk structure of Pt$_5$Ce is constituted by the alternate stacking of Pt$_{0.66}$Ce$_{0.33}$ and Pt layers, it is feasible that the observed Pt−Ce alloy constitutes the interface over which the metal particle grows.

By inspection of Figure 12a, it can be seen that in a reductive environment an abrupt change of lattice constant occurs, demonstrating that bulk reduction in r-Pt1CZ is much more straightforward than that in c-Pt1CZ. Moreover, bulk reduction in r-Pt1CZ takes place with an induction time that is not observed, under the same experimental conditions, in r-CZ. Therefore, permeation of the tubes by the reagent gas cannot be the main source of delay in the observed structural transition. Taking into account that in all of the OSCC experiments the CO conversion starts as soon as the CO/He mixture reaches the catalyst, it is likely that the initial step of CO oxidation over r-Pt1CZ involves the consumption of surface oxygen, either adsorbed or structural. The latter process brings about the reduction of surface or subsurface Ce(IV),[5] which does not produce a modification of bulk lattice constant. After the oxygen depletion of the support surface layer, bulk reduction takes place, and, as demonstrated by the presence of two phases, one reduced and one still oxidized (Figure 10), it is accomplished by the propagation of a reduction front. This interpretation is supported also by the behavior of the fwhm: the sharp fwhm peak during

reduction (Figure 12b) is likely originated by the smaller size of the coherently scattering domains during transition, due to the presence of two distinct phases within the same particle; also lattice mismatch, with the consequent strain at the boundary between the two phases, may contribute to the steep increase of fwhm. During the structural transition to the reduced state, this effect is competitive with the above-described strain release, while, during oxidation, it adds to the mechanism of strain formation induced by the recovery of the Ce(IV) oxidation state.

In r-CZ, the induction time, the steep variation of the lattice constant, and the presence of two phases during reduction are not observed. Although some difference in the structure of the bulk could be recognized, it is clear that the major difference between r-CZ and r-Pt1CZ consists of the surface composition: while in r-Pt1CZ the presence of supported Pt enhances the release of $CO_2$ and therefore the availability of catalytic sites for further CO oxidation, in r-CZ the turnover of reactants is not equally straightforward.[35] As a consequence, bulk reduction is slower, allowing the uniform bulk diffusion of oxygen vacancies and the detection by XRD of a single phase corresponding to an average reduction state. Further support for this analysis comes from the observation that, during oxidation, the in situ powder patterns of both r-CZ and r-Pt1CZ behave in a very similar way, showing the simultaneous presence of reduced and oxidized phase and a steep increase of the FWMH (Figures 11a and 12a). Moreover, the asymptotic lattice parameter value (~5.36 Å) is about the same for both materials in the reduced state. Overall, we can conclude that bulk properties of r-CZ and r-Pt1CZ are similar and that the unlikely behavior in CO reduction could be attributed to the different surface reactivity.

It is not possible to set quantitative relationships between the TPR-OSCC data and the evidence obtained by structural investigations, because the respective experimental setups are quite different. However, the low reduction temperature observed by CO-TPR and the fast process of bulk reduction determined by in situ XRD seem to be strictly correlated; further investigations are needed to determine the relative extent of CO oxidation by bulk oxygen with respect to other possible reactions paths such as CO disproportionation.[35] The similar reduction temperature (Figure 3) of c-Pt1CZ and of r-Pt1CZ points to a similar beneficial effect of Pt in both materials. However, it is hard to draw general conclusions concerning the metal−support interaction in the two samples, because c-Pt1CZ is intrinsically nonhomogeneous and probably shows a behavior that is a weighted average corresponding to different microstructures. On the other hand, EXAFS analysis demonstrated that in r-Pt1CZ a kind of strong metal−support interaction is effective: a Pt−Ce alloy seems to be the interface between Pt metal particles and ceria-zirconia. The stability of size and oxidation state of the Pt particles is likely due to this interaction. Although direct evidence is not available, also the reactivity should be influenced by this interaction, as demonstrated by the OSCC value, which is almost twice that of c-Pt1CZ. In this respect, both of the hypotheses, that CO oxidation sites are located at the boundary between Pt particles and the mixed oxide or that the Pt particles in tight interaction with the support modify its chemical reactivity, are plausible.

## Conclusions

Pt supported on ceria-zirconia gives rise to peculiar properties of the resulting composite material: (i) $CO_2$ coming from anaerobic CO oxidation is produced in larger amount and at lower temperature with respect to metal free ceria-zirconia; (ii) redox-aged Pt/ceria-zirconia shows evidence of a direct Pt−Ce interaction; and (iii) bulk reduction is much faster and starts with an induction time with respect to CZ. In this paper, it is proposed that the reduction mechanism of r-Pt1CZ consists of two steps: initially, the preferential reduction of the support surface takes place; afterward, bulk reduction is accomplished. As demonstrated by in situ XRD, the overall lattice oxygen amount that r-CZ and r-Pt1CZ can deliver at 773 K for the oxidation of CO is about the same for the two materials. The much faster bulk reduction observed by in situ XRD for r-Pt1CZ has been attributed to a beneficial effect of the supported metal, and in particular to an easier release of reacted $CO_2$, producing a more effective turnover of reactants at the catalyst surface. The formation of a Pt−Ce alloy, demonstrated by EXAFS analysis, is the source of the size and oxidation state stability of the Pt metal particles in r-Pt1CZ and, in all probability, also of the peculiar reactivity properties of redox-aged Pt/ceria-zirconia.

## References and Notes

(1) Kašpar, J.; Fornasiero, P.; Hickey, N. *Catal. Today* **2003**, *77*, 419.

(2) Holmgren, A.; Andersson, B. *J. Catal.* **1998**, *178*, 14.

(3) Bozo, C.; Guilhaume, N.; Herrmann, J.-M. *J. Catal.* **2001**, *203*, 393.

(4) Mamontov, E.; Egami, T.; Brezny, R.; Koranne, R.; Tyagi, T. *J. Phys. Chem. B* **2000**, *104*, 11110.

(5) Daturi, M.; Finocchio, E.; Binet, C.; Lavalley, J.-C.; Fally, F.; Perrichon, V.; Vidal, H.; Hickey, N.; Kašpar, J. *J. Phys. Chem. B* **2000**, *104*, 9186.

(6) Hardacre, C.; Roe, G. M.; Lambert, R. M. *Surf. Sci.* **1995**, *326*, 1.

(7) Bernal, S.; Calvino, J. J.; Cauqui, M. A.; Gatica, J. M.; López Cartes, C.; Pérez Omil, J. A.; Pintado, J. M. *Catal. Today* **2003**, *77*, 385.

(8) Bunluesin, T.; Gorte, R. J.; Graham, G. W. *Appl. Catal., B* **1998**, *15*, 107.

(9) Tibiletti, D.; Bart de Graaf, E. A.; Pheng Teh, S.; Rothenberg, G.; Farrusseng, D.; Mirodatos, C. *J. Catal.* **2004**, *225*, 489.

(10) Fu, Q.; Saltsburg, H.; Flytzani-Stephanopoulos, M. *Science* **2003**, *301*, 935.

(11) Bernal, S.; Calvino, J. J.; Cauqui, M. A.; Gatica, J. M.; Larese, C.; Pérez Omil, J. A.; Pintado, J. M. *Catal. Today* **1999**, *50*, 175.

(12) Golunski, S. E.; Hatcher, H. A.; Rajaram, R. R.; Truex, T. J. *Appl. Catal., B* **1995**, *5*, 367.

(13) Liotta, L. F.; Longo, A.; Macaluso, A.; Martorana, A.; Pantaleo, G.; Venezia, A. M.; Deganello, G. *Appl. Catal., B* **2004**, *48*, 133.

(14) Vlaic, G.; Fornasiero, P.; Geremia, S.; Kašpar, J.; Graziani, M. *J. Catal.* **1997**, *168*, 386.

(15) Fonda, E.; Colavita, D.; Andreatta, P. E.; Vlaic, G. *J. Synchrotron Radiat.* **1999**, *6*, 34.

(16) Bera, P.; Priolkar, K. R.; Gayen, A.; Sarode, P. R.; Hegde, M. S.; Emura, S.; Kumashiro, R.; Jayaram, V.; Subbanna, G. N. *Chem. Mater.* **2003**, *15*, 2049.

(17) Bitter, J. H.; Cauqui, M. A.; Gatica, J. M.; Bernal, S.; Ramaker, D. E.; Koningsberger, C. D. *Stud. Surf. Sci. Catal.* **2000**, *130*, 3183.

(18) Longo, A.; Balerna, A.; d'Acapito, F.; D'Anca, F.; Giannici, F.; Liotta, L. F.; Pantaleo, G.; Martorana, A. *J. Synchrotron Radiat.* **2005**, *12*, 499.

(19) Boaro, M.; de Leitenburg, C.; Dolcetti, G.; Trovarelli, A. *J. Catal.* **2000**, *193*, 338.

(20) Ozawa, M.; Loong, C.-K. *Catal. Today* **1999**, *50*, 329.

(21) Rodriguez, J. A.; Hanson, J. C.; Kim, J.-Y.; Liu, G.; Igesias-Juez, A.; Fernandez-Garcia, M. *J. Phys. Chem. B* **2003**, *107*, 3535.

(22) Martorana, A.; Deganello, G.; Longo, A.; Prestianni, A.; Liotta, L. F.; Macaluso, A.; Pantaleo, G.; Balerna, A.; Mobilio, S. *J. Solid State Chem.* **2004**, *177*, 1268.

(23) Kim, D. J. *J. Am. Ceram. Soc.* **1989**, *72*, 1415.

(24) Liotta, L. F.; Macaluso, A.; Longo, A.; Pantaleo, G.; Martorana, A.; Deganello, G. *Appl. Catal., A* **2003**, *240*, 295.

(25) Bedrane, S.; Descorme, C.; Duprez, D. *Catal. Today* **2002**, *75*, 233.

(26) Filipponi, A.; Di Cicco, A.; Natoli, C. R. *Phys. Rev. B* **1995**, *52*, 15122.

(27) Filipponi, A.; Di Cicco, A. *Phys. Rev. B* **1995**, *52*, 15135.

(28) James, F. *MINUIT Function Minimization and Error Analysis*; CERN Program Library Long Write-up D506, CERN Geneva, Switzerland, 1994.

(29) Martorana, A.; Deganello, G.; Longo, A.; Deganello, F.; Liotta, L. F.; Macaluso, A.; Pantaleo, G.; Balerna, A.; Meneghini, C.; Mobilio, S. *J. Synchrotron Radiat.* **2003**, *10*, 177.

(30) Larson, A. C.; Von Dreele, R. B. *GSAS, The General Structure Analysis System*; Los Alamos National Laboratory, 1991−2001.

(31) Nagai, Y.; Yamamoto, T.; Tanaka, T.; Yoshida, S.; Nonaka, T.; Okamoto, T.; Suda, A.; Sugiura, M. *Catal. Today* **2002**, *74*, 225.

(32) Fornasiero, P.; Montini, T.; Graziani, M.; Kašpar, J.; Hungría, A. B.; Martínez-Arias, A.; Conesa, J. C. *Phys. Chem. Chem. Phys.* **2002**, *4*, 149.

(33) Fornasiero, P.; Balducci, G.; Di Monte, R.; Kašpar, J.; Sergo, V.; Gubitosa, G.; Ferrero, A.; Graziani, M. *J. Catal.* **1996**, *164*, 173.

(34) Balducci, G.; Kašpar, J.; Fornasiero, P.; Graziani, M.; Islam, M. S.; Gale, J. D. *J. Phys. Chem. B* **1997**, *101*, 1750.

(35) Arena, G. E.; Centi, G.; Deganello, G.; Liotta, L. F.; Macaluso, A.; Pantaleo, G. *Top. Catal.* **2004**, *30/31*, 397.

(36) Balerna, A.; Liotta, L. F.; Longo, A.; Martorana, A.; Meneghini, C.; Mobilio, S.; Pipitone, G. *Eur. Phys. J. D* **1999**, *7*, 89.

(37) McCabe, R. W.; Wong, C.; Woo, H. S. *J. Catal.* **1988**, *114*, 354.

(38) Li, T.; Balbuena, P. B. *J. Phys. Chem. B* **2001**, *105*, 9943.

(39) Janin, E.; von Schenck, H.; Göthelid, M.; Karlsson, U. O.; Svensson, M. *Phys. Rev. B* **2000**, *61*, 13144.

(40) Vidal, H.; Bernal, S.; Kašpar, J.; Pijolat, M.; Perrichon, V.; Blanco, G.; Pintado, J. M.; Colon, G.; Fally, F. *Catal. Today* **1999**, *54*, 93.

(41) Adroja, D. T.; Malik, S. K.; Padalia, B. D.; Vijayaraghavan, R. *Solid State Commun*. **1989**, *71*, 649.